Journal of Materials Chemistry A

ROYAL SOCIETY OF CHEMISTRY

PAPER

View Article Online
View Journal

Check for updates

Cite this: DOI: 10.1039/d5ta07228j

Strain engineering of ScN thin films and its effect on optical, electrical, and thermoelectric properties

Arnaud le Febvrier, *[a] Sanath Kumar Honnali, [a] Charlotte Poterie, [b] Tiago V. Fernandes, [a] Robert Frost, [c] Vladyslav Rogoz,[d] Martin Magnuson,[d] Fabien Giovannelli,[e] Joaquim P. Leitão, [f] Jean Francois Barbot[b] and Per Eklund [ad]

Scandium nitride (ScN) is a cubic NaCl-structured, degenerate, narrow-bandgap, n-type semiconductor that exhibits remarkable semiconducting, thermoelectric and plasmonic properties. However, its properties are sensitive to several types of defects, such as crystal defects, morphology, intentional or unintentional doping. For the purpose of reducing the deposition temperature of ScN, a series of films were deposited in the temperature range of 250–850 °C using a high-power impulse magnetron sputtering technique. While the stoichiometry and crystal structure remained unaffected in the sample series, the optical and electrical properties were affected when the temperature was decreased. Using in-depth XRD, optical and electrical characterizations, the effect of strain and dislocations on the semiconductor properties of ScN was evaluated. A reduction in the deposition temperature from 850 °C to 450 °C yielded a slow change in the electrical and optical properties, while a drastic change occurred for the films deposited below 450 °C. The main cause of the deterioration of the electrical transport properties (σ/10 000; n/100, and μ/100) was attributed to a high dislocation density (10^{11} cm^{-2}) along with a rhombohedral distortion of the ScN cell (α: 90° → 88.6°), which was the main cause of the variation in the electrical transport. The presence of dislocations/crystal defects in the film generated defect states near the edges of the valence and conduction bands, softening the edges and impacting the electron density and mobility. The best thermoelectric properties of ScN were obtained when it was grown at 850 °C and were further modified and altered by strain engineering.

Received 4th September 2025
Accepted 17th November 2025

DOI: 10.1039/d5ta07228j

rsc.li/materials-a

Open Access Article. Published on 03 December 2025. Downloaded on 12/8/2025 11:38:25 AM.
This article is licensed under a Creative Commons Attribution 3.0 Unported Licence.

1 Introduction

Scandium nitride is a transition metal nitride exhibiting remarkable semiconducting phonon–polariton, electrical, and piezoelectric applications.[1,2] ScN also serves as a seed layer in the semiconductor industry for enhancing the performance of GaN devices used in metal/semiconductor superlattices.[3–5] In the last few decades, scandium nitride and its derivatives that are used for solid solutions, doping, and superlattices have been investigated for their promising thermoelectric properties.[6–11] Thermoelectric materials allow for the direct conversion of thermal energy into electricity using the Seebeck effect. The thermoelectric performance is defined by the figure of merit:

$$ZT = \frac{S^2\sigma}{(\kappa_e + \kappa_l)}T \quad (1)$$

where S is the Seebeck coefficient, σ is the resistivity, κ_e is the electronic component of the thermal conductivity, κ_l is the lattice component of the thermal conductivity and T is the absolute temperature.[12] An improvement of the figure of merit often arises from a reduction of the thermal conductivity while maintaining favorable electrical transport properties *via* maximizing the thermoelectric (TE) power factor ($S^2\sigma$).

Scandium nitride (ScN) is a NaCl-structured, degenerate, narrow-bandgap, n-type semiconductor with an indirect bandgap of ~0.9 eV and a direct bandgap estimated at around 2.6 eV. The electrical and thermoelectric properties of this material are sensitive to defects, such as crystal defects, morphological changes, intentional or unintentional doping. As an example, its electrical conductivity can vary between 4×10^3 and 5×10^6 S cm^{-1}; its carrier concentration varies from 10^{19} to 10^{21} cm^{-3};[7,13,14] and its carrier mobility can vary between 0.2 to 150 cm^2 V^{-1} s^{-1}.[7–11,13,15] Similarly, its thermoelectric properties also vary greatly. In the best case, it is a promising

[a]Inorganic Chemistry, Department of Chemistry–Ångström Laboratory, Uppsala University, SE-751 21 Uppsala, Sweden. E-mail: arnaud.lefebvrier@kemi.uu.se
[b]PPRIME Institute, CNRS, Université de Poitiers–ENSMA, UPR 3346, SP2MI, TSA 41123, 86073 Poitiers Cedex 9, France
[c]Department of Physics and Astronomy, Uppsala University, SE-751 21 Uppsala, Sweden
[d]Department of Physics, Chemistry and Biology (IFM), Linköping University, SE-581 83 Linköping, Sweden
[e]Laboratoire GREMAN, CNRS, Université de Tours, UMR 7347, 41029 Blois, France
[f]i3N and Departamento de Física, Universidade de Aveiro, Aveiro, 3810-193, Portugal

Open Access Article. Published on 03 December 2025. Downloaded on 12/8/2025 11:38:25 AM. This article is licensed under a Creative Commons Attribution 3.0 Unported Licence.

thermoelectric material. Studies have reported thermoelectric properties with Seebeck coefficients of −40 and −70 μV K^{-1} at 300 K[8–11,15] and maximal TE power factors between 0.1 and 2 mW m^{-1} K^{-2} at room temperature, with larger values up to 3.5 mW m^{-1} K^{-2} at higher temperatures (400–600 °C).[7,9–11,13,16] These values can be compared with those of PbTe and Bi_2Te_3, which are benchmark thermoelectric materials that have power factors reaching up to 2.0 mW m^{-1} K^{-2} at 250–550 °C[17] and 4.5 mW m^{-1} K^{-2} around 100 °C,[18] respectively.

ScN thin films can be deposited using reactive magnetron sputtering[9,11,15,19,20] or molecular beam epitaxy.[3,7,13] Of these techniques, magnetron sputtering is the most often used for growing ScN and is widely used for applications in hard coatings to the semiconductor industry. One of the common ways of growing ScN films is by reactive direct current magnetron sputtering (dcMS) at high-deposition temperatures.[9–11,15,16] However, in recent years, pulsed magnetron discharges, such as high-power impulse magnetron sputtering (HiPIMS), have typically been used for modifying the film morphology, crystallographic orientation, and stress, and to control defects in functional thin films such as CrN, AlN, and AlScN.[21–24]

HiPIMS enables ionization of the sputtered species by an electron-impact ionization process, where the average energy of the ionized species is in the range of a few tens of eV.[25] This is in contrast to neutral metallic flux, which is thermalized (1–3 eV), as observed in dcMS.[26] This highly ionized and energetic metal ion flux has been the key tool for reducing the growth temperature, while providing sufficient energy for the adatoms to promote the crystallization of the materials, which is equivalent to growing films at high temperatures.[27,28] Reducing the deposition temperature is of interest from technological aspects, such as the use of polymeric substrates or for complex, layer-stacked growth, where the underlying layers are temperature sensitive. These properties are highly attractive for growing dense nitride, oxide, or carbide thin films for various applications, such as hard coatings, optical reflectors, diffusion barrier coatings, and metastable oxide layers.[29–32]

The composition of the films grown in the reactive HiPIMS process is generally better controlled by choosing the process point from the shape of the discharge peak current.[33] This enhances the reproducibility of stoichiometric films; however, non-stoichiometric films are often reported (under the same discharge and reactive gas conditions) with dc discharges due to resputtering, target poisoning effects and reactivity towards the metal ion.[34,35] Since HiPIMS allows for the growth of dense films, it is possible to minimize the incorporation of contaminants, which is otherwise observed in films deposited with a less energetic discharge, such as dcMS.[36] However, there are a few drawbacks of using HiPIMS discharges, such as a low-deposition rate and high residual stress in the films.[37,38] The residual stress generated in the HiPIMS-grown films is attributed to the generation of point defects as well as compositional and morphological changes. The stress can be a significant factor for hard-coating applications, where the higher mechanical strength could be due to strain-induced hardening or from the films being harder than those of the same material grown by other techniques.[39]

The stress and strain levels present in the synthesized film are often overlooked properties for the thermoelectric application of semiconducting thin films, but they are necessary for understanding their impact on electrical properties. In the present study, we examine the reduction in the deposition temperature of a degenerate ScN semiconductor, which is usually grown at temperatures higher than 800 °C.[9,11,13,15] ScN was chosen for the following reasons: (i) the high temperature needed for its synthesis, (ii) its original optical properties, (iii) its promising properties for thermoelectricity, and (iv) its electrical and thermoelectric properties are highly sensitive to external factors. We focus on the impact of temperature on the generated stress/strain in the film, and consequently on its physical properties. The variation in the optical, electrical, and thermoelectric properties is discussed in connection with detailed structural and composition analyses.

2 Experimental details

2.1 Material synthesis

The ScN_x films were grown by reactive magnetron sputtering in an ultra-high vacuum chamber (base pressure $\sim 10^{-7}$ Pa).[40] The depositions were done in a single unbalanced magnetron configuration to increase the ion assistance and eliminate the magnetic cross-coupling of the plasma present in a tilted closed-field configuration with four magnetrons.[41] The magnetron assembly with a scandium (Sc) target of 50.8 mm (2-inch diameter, 99.95% purity, Mateck) was situated ∼14 cm away at an angle of 30° from the normal of the substrate. The target was sputtered in a mixed Ar/N_2 atmosphere at a constant deposition pressure of 0.33 Pa (2 mTorr) with a constant N_2 and Ar flow rate at 15 sccm (∼33%) and 30 sccm, respectively. The deposition time was kept constant at 75 min for all the depositions, which yielded a film thickness in the range of 220–260 nm. Prior to each deposition, the target was sputter-cleaned for 5 min in Ar atmosphere at ∼0.2 Pa (1.5 mTorr).

The films were deposited using a unipolar HiPIMS at an average constant power of 110 W. The unipolar HiPIMS pulses were generated by a HiPSTER 1 unit (Ionautics AB, Sweden) with a 50 μs pulse width (τ_{on}). The pulsing frequency was adjusted between 540–610 Hz to maintain a target peak current I_{pk} of ∼21 A. The N_2 flow ratio of 33% was selected based on the triangular shape of the I_{pk}, which indicated an operation under a poisoned mode.[33] The films were grown on two-sided polished, *c*-plane cut sapphire and on SiO_2 (200 nm)/Si(100) substrates with a dimension of 10 mm × 10 mm × 0.5 mm. The substrates were ultrasonically cleaned in acetone and ethanol for 10 minutes and blown dry with nitrogen (N_2) gas. During deposition, the substrates were electrically floating ($V_{float} \approx -25$ V) under a constant rotation of 15 rpm with no substrate etching. The substrate temperature (T_s) was fixed at different temperatures from 250 to 850 °C.

2.2 Material characterization

The elemental composition of the films was measured by time-of-flight elastic recoil detection analysis (ToF-ERDA). The

 This journal is © The Royal Society of Chemistry 2025

Open Access Article. Published on 03 December 2025. Downloaded on 12/8/2025 11:38:25 AM. This article is licensed under a Creative Commons Attribution 3.0 Unported Licence.

measurements were carried out using a Pelletron Tandem accelerator (5 MV NEC-5SDH-2) at the Tandem Laboratory, Uppsala University, Sweden.[42] The measurements were conducted using a 36 MeV primary iodine ion ($^{127}I^{8+}$) beam. The angle of the incident beam relative to the target surface normal was 67.5°, while a ToF-telescope and a gas ionization detector were placed at 45° relative to the direction of the incident beam. The depth profile of the elemental composition was acquired from the ToF-ERDA time and energy coincidence spectra using the Potku (version 2.2) code.[43]

X-ray diffraction (XRD) measurements were performed on a PANalytical X'Pert PRO diffractometer in a Bragg–Brentano (θ–2θ) geometry, with Cu Kα (λ = 1.540598 Å) radiation and a Ni filter. The recorded 2θ range was 10–90° with a step size of 0.008° and an equivalent time per step of 19 s using the PIXcel 1D detector. The film thickness, density and roughness were estimated by X-ray reflectivity (XRR), which was performed using a Philips X'Pert MRD diffractometer equipped with an X-ray mirror with a 1/32° slit as the incident optics and a parallel plate collimator (0.18°) with a detector. Pole figures were acquired with a polycapillary with crossed slits (4 mm^2) as the primary optics and a parallel plate collimator (0.18°) with a flat diffracted beam monochromator as the secondary optics with a proportional Xe1 detector. Reciprocal space maps (RSM) of the symmetric 111 peak and the asymmetric 113 peak of ScN were acquired on the same type of diffractometer equipped with a hybrid mirror as the primary optics and a PiXcel^{2D} detector for fast acquisition with no particular optics for the receiving optics.

The XPS data were obtained using an Axis Ultra DLD instrument from Kratos Analytical (UK) with a base pressure of 1.1×10^{-9} Torr (1.5×10^{-7} Pa) during spectra acquisition and monochromatic Al K_α radiation ($h\nu$ = 1486.6 eV). The anode power was set to 150 W. Prior to analyses, all samples were sputter-cleaned with a 0.5 keV Ar^+ ion beam incident at an angle of 20° from the surface and rastered over an area of 3 × 3 mm^2. All spectra were collected from an area of 0.3 × 0.7 mm^2 and at a normal emission angle using a low-energy electron gun to compensate for sample charging. The analyzer pass energy was set to 20 eV, which resulted in a full width at half maximum (FWHM) of 0.55 eV for the Ag $3d_{5/2}$ peak. The XPS data were treated using KolXPD 1.8 fitting software. Peak fitting was performed after applying a Shirley background and the following restrictions: (i) fixed Gauss–Lorentzian peak profiles were used to model the different components in Sc 2p; (ii) the spin-orbital splitting of the Sc 2p peak was respected for all different components with an intensity ratio fixed between the $2p_{3/2}$ and $2p_{1/2}$ peaks and (iii) the relative distance between the Sc $2p_{3/2}$ and Sc $2p_{1/2}$ peaks was fixed at 4.39 eV; (iv) three components were used to model the Sc 2p peak with a nitride component, an oxynitride component, and a substoichiometric $ScN_{1-\delta}$ component at a lower binding energy; (v) fixed Gauss Lorentzian peak profiles were used to model the N 1s peak using one nitride component with a fixed FWHM of 1 eV and an oxynitride component at a higher binding energy with an energy separation between the different components of 1.25 eV.

Transmittance measurements were carried out using a Bruker Vertex 80v Fourier-transform infrared (FTIR) spectrometer equipped with Si and InGaAs detectors. Each sample was positioned perpendicularly to the optical beam path between the light emission of a VIS-NIR source and the detectors at room temperature under ambient atmosphere. The transmitted light through each sample was measured, and the light source's emission spectrum was obtained independently beforehand. The transmittance spectra were then automatically obtained by normalizing the transmitted light to the emission spectrum of the light source.

The in-plane electrical conductivity $\sigma(T)$, charge carrier concentration $n(T)$ and the mobility $\mu(T)$ were measured using an ECOPIA HMS-5500 which combines the van der Pauw method with the Hall effect. The high-temperature setup was used for the temperature-dependent measurements between 300 to 500 K, ensuring operation below the lowest deposition temperature. In the case of the room-temperature measurements, a cryostat setup was used. The mobility (μ) was calculated using σ and n using $\mu_{300\ K} = \frac{\sigma_{300\ K}}{n_{300\ K} \times e}$, where e is the elementary charge. A constant magnetic field of 0.580 T was applied for the Hall measurements. The in-plane Seebeck coefficient was measured under a low-pressure (0.9 atm) helium atmosphere using a ULVAC-RIKO ZEM3 system from 50 °C (323 K) up to a maximum temperature of 225 °C (498 K), corresponding to a temperature below the lowest deposition temperature.

To test the recovery and the temperature stability of the film deposited at the lowest temperature, a post-annealing test was conducted at 1300 °C for 10 min in a purpose-built lamp furnace under a vacuum of 5×10^{-6} Pa.

First-principles calculations were performed within the framework of density functional theory (DFT) using the Vienna *Ab initio* Simulation Package (VASP).[44,45] The projector augmented-wave (PAW) method[46] was employed to treat core–valence interactions, and a plane-wave energy cutoff of 700 eV was used. To investigate the effect of lattice distortion on the electronic properties of scandium nitride (ScN), the conventional face-centered cubic unit cell was transformed into a reduced Niggli cell. The transformation included a small angular distortion of 1.4°, resulting in a monoclinic cell oriented along the space diagonal of the conventional cubic cell. This approach allows for symmetry breaking, removes degeneracies and band folding in the electronic structure, thereby enabling a more accurate analysis of bandgap changes due to structural distortions. For the exchange–correlation functional, the HSE06 screened hybrid functional[47,48] was applied to accurately describe the electronic band structure and the bandgap of ScN. The HSE06 method includes 25% of the short-range Hartree–Fock exchange mixed with 75% of the PBE exchange, and uses a screening parameter of 0.2 Å^{-1}. This hybrid approach was essential for capturing the correct magnitude and trends of the bandgap, which are underestimated by conventional functionals, such as GGA or GGA + U. In particular, the bandgap response to structural distortion was found to be highly dependent on the choice of the functional, with GGA + U

Open Access Article. Published on 03 December 2025. Downloaded on 12/8/2025 11:38:25 AM.
This article is licensed under a Creative Commons Attribution 3.0 Unported Licence.

proving insufficient for reliably describing the system. The use of HSE06 was therefore critical, albeit at a higher computational cost. For the band structure calculations using HSE06, an explicit list of 106 *k*-points was applied with the reduced cubic ScN Niggli unit cell comprising one Sc and one N atom.

3 Results

3.1 Composition

Table 1 lists the elemental composition of the films determined by ToF-ERDA along with the base pressure in the UHV chamber at the deposition temperatures. All the films contained a level of contamination (O, F, C) at the detection limit of ToF-ERDA. Regardless of the deposition temperature and substrate, all the films had a close-to-stoichiometry composition within the error bar (Table 1 and S1 for the films deposited on the SiO_2 (200 nm)/Si substrate). The ToF-ERDA elemental depth profiles also confirm that the SiO_2 layer initially present on the Si substrate was thick enough to electrically insulate the films from the substrate and remained intact even at the highest substrate temperature of 850 °C (Fig. S1). In this study, these results show that HiPIMS allowed for a better control over the growth of the stoichiometric ScN, which was achieved even at low temperatures; these results are in contrast with those of the commonly used dcMS, which can lead to different N/Sc ratios and oxygen contamination in the film when grown at different T_s.[6,10,11,15,49,50]

The results of the XPS analysis (Fig. S2, SI) show that the samples in the series were relatively similar to each other in terms of their compositions, core level signatures and valence band signature. Only minor variations can be reported, such as the shift of +0.2 eV of the nitride component in the Sc $2p_{3/2}$ core level, as well as the small increase of one of the valence features (hybridization of N 2p-Sc 3d) at 5.6 eV, which occurred when the deposition temperature was increased to 850 °C.

3.2 Structural characterization

The X-ray reflectivity analysis performed on the two series of samples revealed the presence of a 3–4 nm thin oxide layer at the top of the film (refer to Fig. S2 and Table S2 in the SI for further details).

Fig. 1 displays the Bragg–Brentano XRD pattern acquired for the series of films deposited on the *c*-sapphire at different

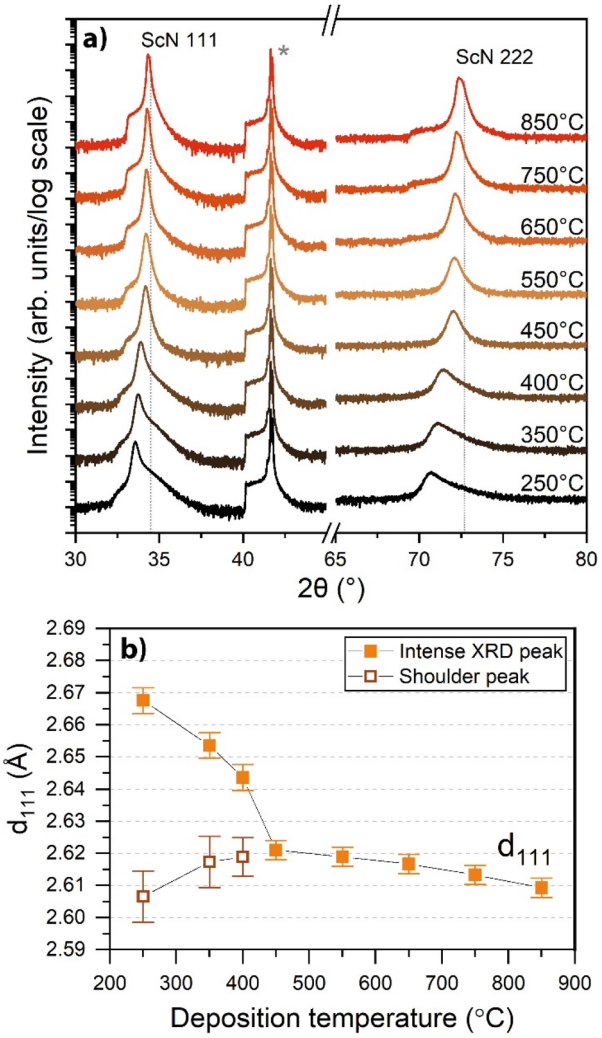

Fig. 1 (a) θ–2θ XRD patterns of the ScN films deposited at different temperatures on *c*-plane sapphire. (b) Temperature-dependence of the out-of-plane (111) lattice distance determined from deconvolution of two XRD peaks at $T_s \leq 400$ °C. A filled symbol corresponds to the intense XRD peaks and an open symbol corresponds to the shoulder peak at a higher angle. Vertical dashed lines correspond to XRD scattering angles of the bulk ScN taken from ICDD 03-065-6286. The 006 Al_2O_3 peak is marked with a * symbol.

Table 1 Elemental composition determined by ToF-ERDA for the series of ScN_x films deposited at different temperatures on a *c*-sapphire substrate. Base pressure at T_s in the UHV chamber is mentioned for each deposited film

		Composition (±0.5 at%)					
T_s (°C)	Base pressure at T_s ($\times 10^{-7}$ Pa)	Sc	N	O	F	C	N/Sc ratio (±0.02)
250	1.7	49.2	49.5	0.77	0.23	0.14	**1.01**
350	2.0	50.3	48.6	0.6	0.19	0.20	**0.97**
400	1.7	50.2	48.6	0.6	0.16	0.18	**0.97**
450	2.3	49.5	49.0	0.9	0.17	0.14	**0.99**
550	2.3	49.3	49.8	0.55	0.14	0.19	**1.01**
650	3.5	49.4	49.6	0.62	0.24	0.24	**1.00**
750	4.8	49.8	49.4	0.54	0.07	0.08	**0.99**
850	30.6	48.9	50.3	0.52	0.11	0.08	**1.03**

This journal is © The Royal Society of Chemistry 2025

Open Access Article. Published on 03 December 2025. Downloaded on 12/8/2025 11:38:25 AM.
This article is licensed under a Creative Commons Attribution 3.0 Unported Licence.

substrate temperatures (T_s). Fig. 1b displays the evolution of the out-of-plane lattice distance *versus* the deposition temperature. Note that two XRD peaks were deconvoluted from the XRD pattern for the low-temperature-deposited films ($T_s \leq 400$ °C); they are represented by a filled symbol for the most intense peak and an open symbol for the shoulder XRD peak at a higher angle.

For the films deposited on *c*-sapphire, only the substrate peaks at 41° and peaks from the (111) family of NaCl-B1 (ScN) were observed, revealing highly oriented films. Upon increasing T_s above 450 °C, the following was observed: (i) d_{111} decreased from 2.62 Å to 2.61 Å; (ii) the peaks became narrower; and (iii) the intensity of the diffraction peak increased, indicating a higher crystallinity and better orientation of the grains along the growth direction. At $T_s \leq 400$ °C, the peak asymmetry was distinguishable, with deconvolution revealing the possible presence of two diffraction peaks whose corresponding lattice distances increased monotonically up to values of around 2.66 Å after a reduction of T_s. Except for the lowest deposition temperatures ($T_s \leq 400$ °C), the measured d_{111} lattice distance values of ScN compared well with the bulk values recorded at 2.62 Å.[20,51] For SiO_2(200 nm)/Si, similar observations on the evolution of the lattice distance and the asymmetry of the peak at lower temperatures were made (refer to Fig. S3 and the SI for further details).

A more in-depth analysis of the film orientation was conducted through pole figure measurements and reciprocal space mapping (RSM). The representative measurements of the pole figures are presented in the SI (Fig. S4). The major difference between the substrates was their film orientation. The films deposited on the *c*-plane sapphire were (111) epitaxial, while the ones deposited on SiO_2 (200 nm)/Si were (111) or (100) fiber-textured depending on T_s. These differences are commonly

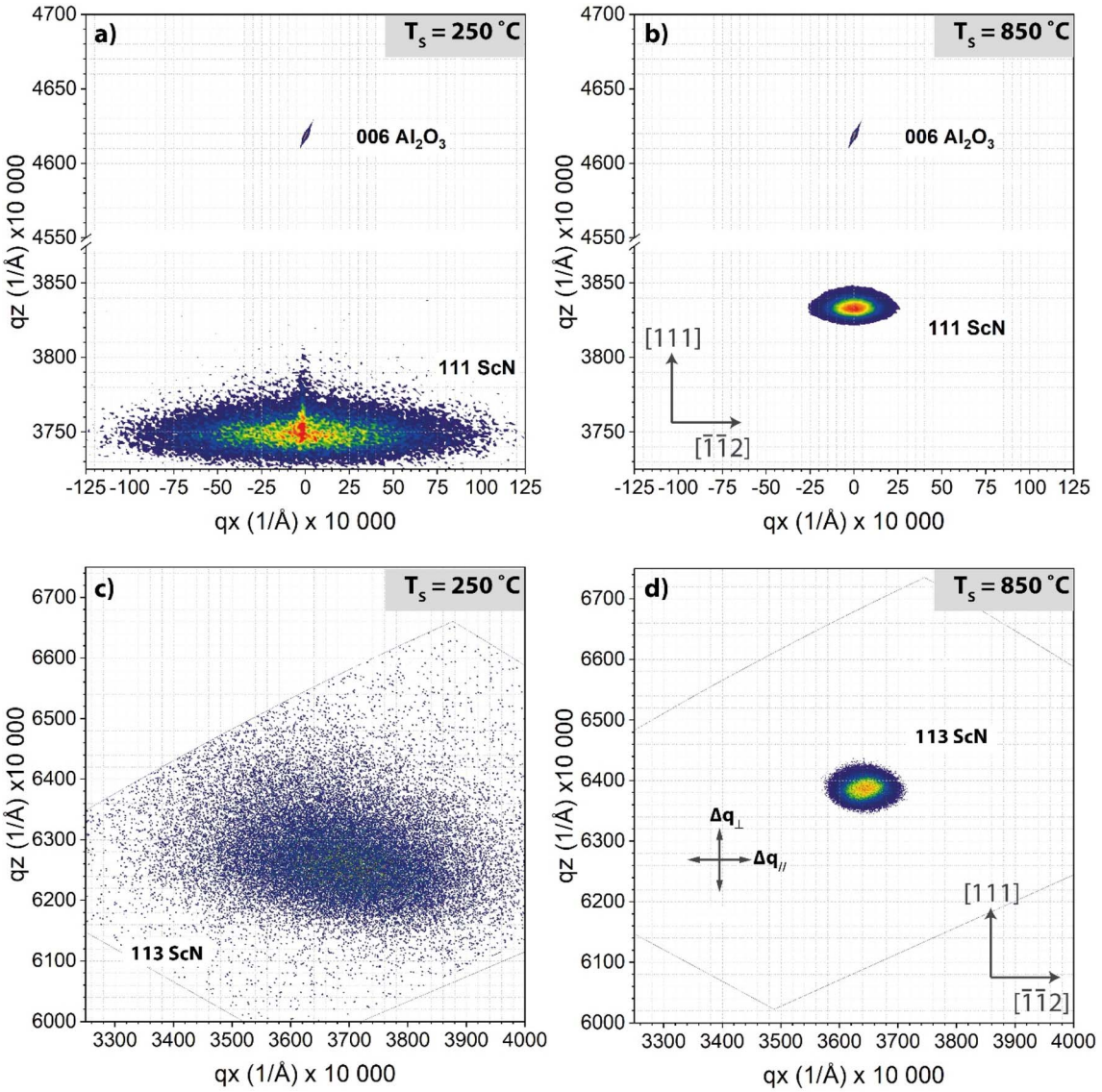

Fig. 2 Reciprocal space map (RSM) of (a and b) the 111 symmetrical peak along with the 006 substrate peak and (c and d) the 113 asymmetric peak measured on the films deposited at (a and c) 250 and (b and d) 850 °C.

Open Access Article. Published on 03 December 2025. Downloaded on 12/8/2025 11:38:25 AM.
This article is licensed under a Creative Commons Attribution 3.0 Unported Licence.

observed in the literature for NaCl-B1 structured materials deposited on those two substrates.[6,15,19,52]

Fig. 2 shows the typical 111 symmetrical and 113 asymmetrical peaks of the ScN films deposited on the *c*-sapphire for the lowest and highest deposition temperatures. Clear differences were observed in the shape and position of the diffraction peak, where a high temperature led to a high crystal quality with no small mosaicity, indicated by the narrow spread of the peak. Low deposition temperatures led to a reduction of the crystal quality and a larger mosaicity of the ScN films. More details on the analysis and the extracted data from all the films are listed in the SI (Table S3). Note that the shape of the asymmetric RSM diffraction spot was relatively circular or ellipsoidal, with no tail, revealing that there was no strain evolution in the film, which could have originated from the film/substrate interface.

Fig. 3 displays the summary of the RSM results, showing the evolution of the structure of ScN and strain *versus* its deposition temperature. Several characteristics of the structure of ScN were extracted from the RSM, such as the cell angles, cell parameters, mosaicity, the out-of-plane lattice distance, the in-plane lattice distance, and the related strain (ε). A clear deviation from an angle of 90° in the cubic system was observed in the series of films (Fig. 3a). The measured cell angle decreased from 89.9° to 88.6° at $T_s = 250$ °C. After the deposition temperature decreased

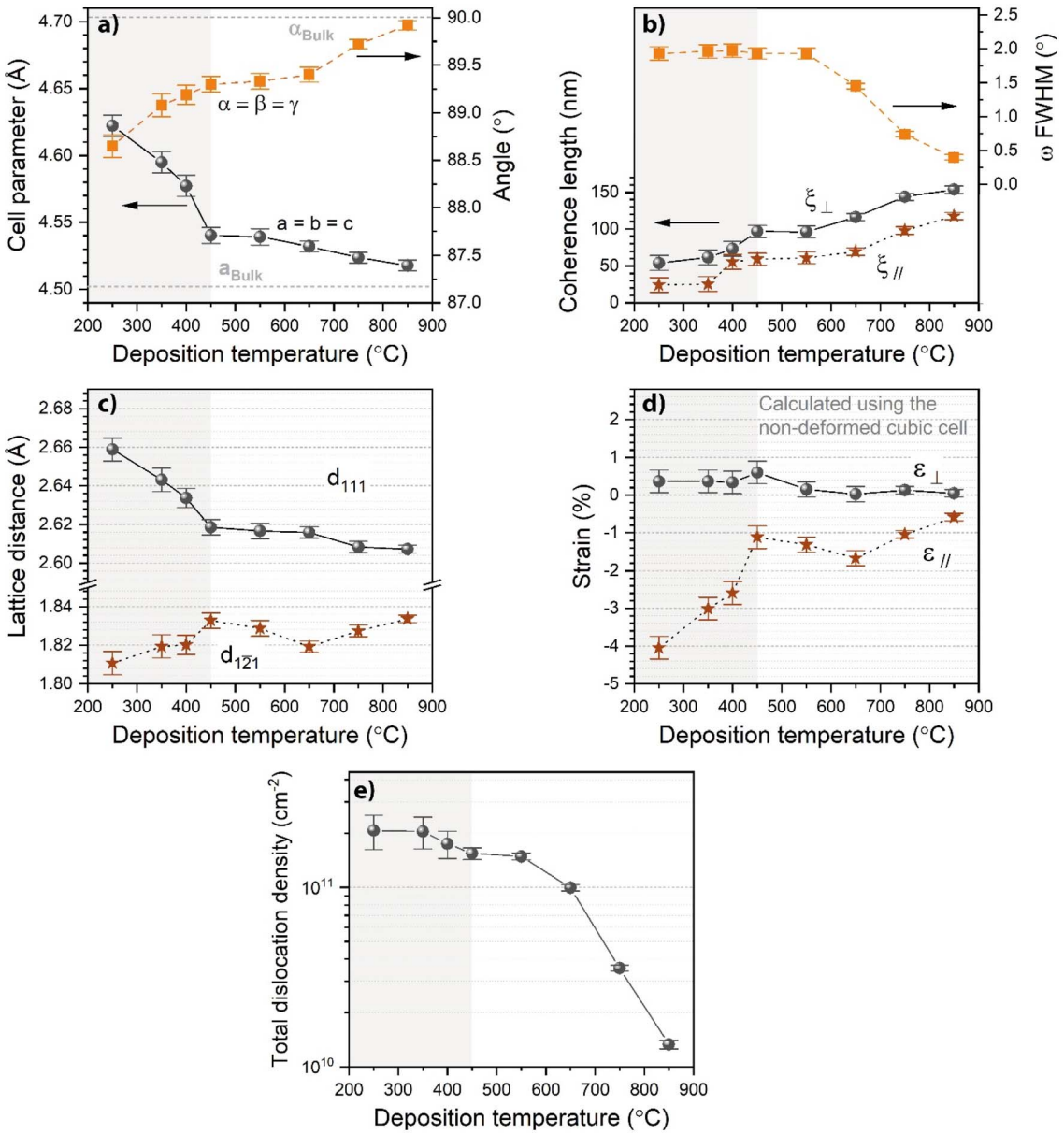

Fig. 3 Evolution *versus* the deposition temperature of the extracted: (a) cell angle and lattice parameters; (b) lateral ($\xi_{\parallel}$) and out-of-plane coherence length ($\xi_{\perp}$), and mosaicity with ω-FWHM of the asymmetric 113 reflection; (c) in-plane and out-of-plane lattice distance; (d) lateral ($\varepsilon_{\parallel}$) and out-of-plane ($\varepsilon_{\perp}$) strain calculated considering a non-deformed cubic cell ($\alpha = \beta = \gamma = 90°$); and (e) extracted upper limit of total dislocation density. The grey zone represents the temperature region for which the cell underwent a pronounced increase in the in-plane strain/deformation.

 This journal is © The Royal Society of Chemistry 2025

Open Access Article. Published on 03 December 2025. Downloaded on 12/8/2025 11:38:25 AM.
This article is licensed under a Creative Commons Attribution 3.0 Unported Licence.

from 850 to 450 °C, the corresponding calculated cell parameter gradually increased from 4.518 Å to 4.540 Å until a sudden increase to a maximum value of 4.62 Å at T_s = 250 °C. For comparison, the bulk unstressed values for ScN has been reported as 4.501 Å.[53]

The mosaicity of the (111) orientation (Fig. 3b), given qualitatively by the evolution of the ω-scan full width at half maximum ($\Delta\omega$ – FWHM) measured in a symmetrical position, increased when the deposition temperature decreased from T_s = 850 °C ($\Delta\omega$ − FWHM = 0.4°) to a maximum for $T_s \leq$ 550 °C ($\Delta\omega$ − FWHM ≈ 2°).

The extracted $\xi_\perp$ was reduced monotonically from 150 nm to values below 50 nm when the deposition temperature was reduced from 850 to 250 °C (Fig. 3b). Similarly, the lateral length ($\xi_\parallel$) with relatively high values around 100 nm for deposition at 850 °C was reduced to values below 20 nm for the films deposited at the lowest temperature.

Fig. 3d displays the calculated strain, considering a relaxed cubic system with its three angles at 90°. The out-of-plane ($\varepsilon_\perp$) strain remained low (0% to +0.3%), while the in-plane ($\varepsilon_\parallel$) strain increased gradually from −0.6% to 1.2% when T_s was reduced from 850 to 450 °C with a maximum strain at T_s = 650 °C with a −1.6% strain value. Below T_s < 450 °C and after a reduction of the deposition temperature, $\varepsilon_\perp$ increased to +0.4% and $\varepsilon_\parallel$ increased gradually from −1% to −4%.

The peak broadening along the rocking-curve direction on the 113 RSM was primarily attributed to the mosaic spread of the single-crystal blocks within the ScN layer. This peak width ($\Delta\omega$) can also be used to estimate an upper limit for the total dislocation density, ρ_D (Fig. 3e), with the following formulae, assuming uncorrelated (randomly distributed) dislocations:[54,55]

$$\rho_D = \frac{\Delta\omega^2}{2\pi \ln 2 \times b^2} \quad (2)$$

$$b = \frac{a_{ScN}}{\sqrt{2}} \quad (3)$$

where $\Delta\omega$ is the peak width in the rocking curve direction for 113 and b is the Burgers vector along the close-packed <110> direction in ScN. The upper limit of the dislocation density that can be present in the film increased when the films were deposited at lower temperatures. At the highest deposition temperature, the total dislocation density was close to 10^{10} cm^{-2} and increased slowly to 10^{11} for the films deposited at 650 °C. For T_s < 650 °C, the values tended to saturate at a total density slightly above 2 × 10^{12} m^{-2}. The presence of dislocations in a material is a signature of its strain release or deformation. In the present case, when the temperature was reduced from 850 to 550 °C, the dislocation density increased and consequently the in-plane strain remained relatively constant and was minimized for those samples. However, for temperatures lower than 450 °C, the dislocation density seemed to have become saturated, while the in-plane strain drastically increased. This observation likely reveals that the ScN material reached a saturation limit of its dislocation density before undergoing a structural deformation and yielding in-plane strain in the films.

3.3 Optical characterization

The light absorption as a function of the photon energy provides valuable information about the electronic energy structure in semiconductor materials. Fig. 4a displays the photographs of the films showing the drastic changes in their visual aspects as the growth temperature was reduced. The transmittance spectra were acquired in the 0.5–3.0 eV range (Fig. S6 in the SI) and were used to extract the absorption coefficient (α) of the spectra. For more details on the treatment of the transmittance data refer to the SI. The absorption coefficient can be used to estimate the optical bandgap ($E_{g,opt}$) of semiconductors,[56,57] based on the Tauc equation given by:

$$(\alpha E)^r = E - E_{g,opt} \quad (4)$$

where E is the photon energy and r is a constant that depends on the nature of the electronic transitions involved in the absorption. Particularly, r takes the value of 2 for allowed direct transitions and 0.5 for allowed indirect transitions.[58] Fig. 4b presents the case when r is set to 2. No evidence for significant absorption, due to the indirect bandgap located at around 0.9 eV, was found (refer to the SI). For clarity, only the Tauc plots of the samples grown at 850 °C and 250 °C are shown. The value of $E_{g,opt}$ was determined by the tangent method and corresponded to an energy where $(\alpha E)^2 = 0$. $E_{g,opt}$ was then plotted as a function of the deposition temperature, as presented in Fig. 4c. Fig. 4b further evidences a region of the sub-bandgap absorption, which was considerably more pronounced for the sample grown at 250 °C. This absorption potentially originated from two distinct mechanisms: the indirect bandgap (~0.9 eV) and/or the defect-induced electronic states. While the indirect transitions are allowed *via* phonon assistance, they are unlikely to change significantly with moderate variations of the growth conditions. In contrast, the growth-induced defects can introduce energy levels inside the bandgap, enabling a stronger sub-bandgap absorption.[59] A sufficiently high density of electronic levels close to the band edges gives rise to tails of the electronic states that extend into the bandgap.

The absorption related to the sub-bandgap electronic states can be studied using Urbach's expression,[60–63] which relates the absorption coefficient (α) to the incident photon energy (E) in the following equation:

$$\alpha = \alpha_0 \exp\left(\frac{E - E_{g,opt}}{E_U}\right) \quad (5)$$

where α_0 is a fitting parameter and E_U is an energy parameter (Urbach energy), which is related to the slope of the band-related absorption edge and determines the width of the electronic states' tails that penetrate the bandgap.[61,63] Additionally, this value is an indicator of the fluctuating potentials present along the semiconductor and is reflected in the fluctuations of the edges of the conduction and valence bands.[62,64] The high-energy applicability limit of eqn (5) is given by $E_{g,opt}$ + 2 E_U.[65]

Fig. 4d shows the absorption coefficient (α) as a function of photon energy (E) for the samples grown at 850 °C and 250 °C. The oscillations in the spectra, more pronounced in the quasi-transparent region, are compatible with optical interference

Open Access Article. Published on 03 December 2025. Downloaded on 12/8/2025 11:38:25 AM.
This article is licensed under a Creative Commons Attribution 3.0 Unported Licence.

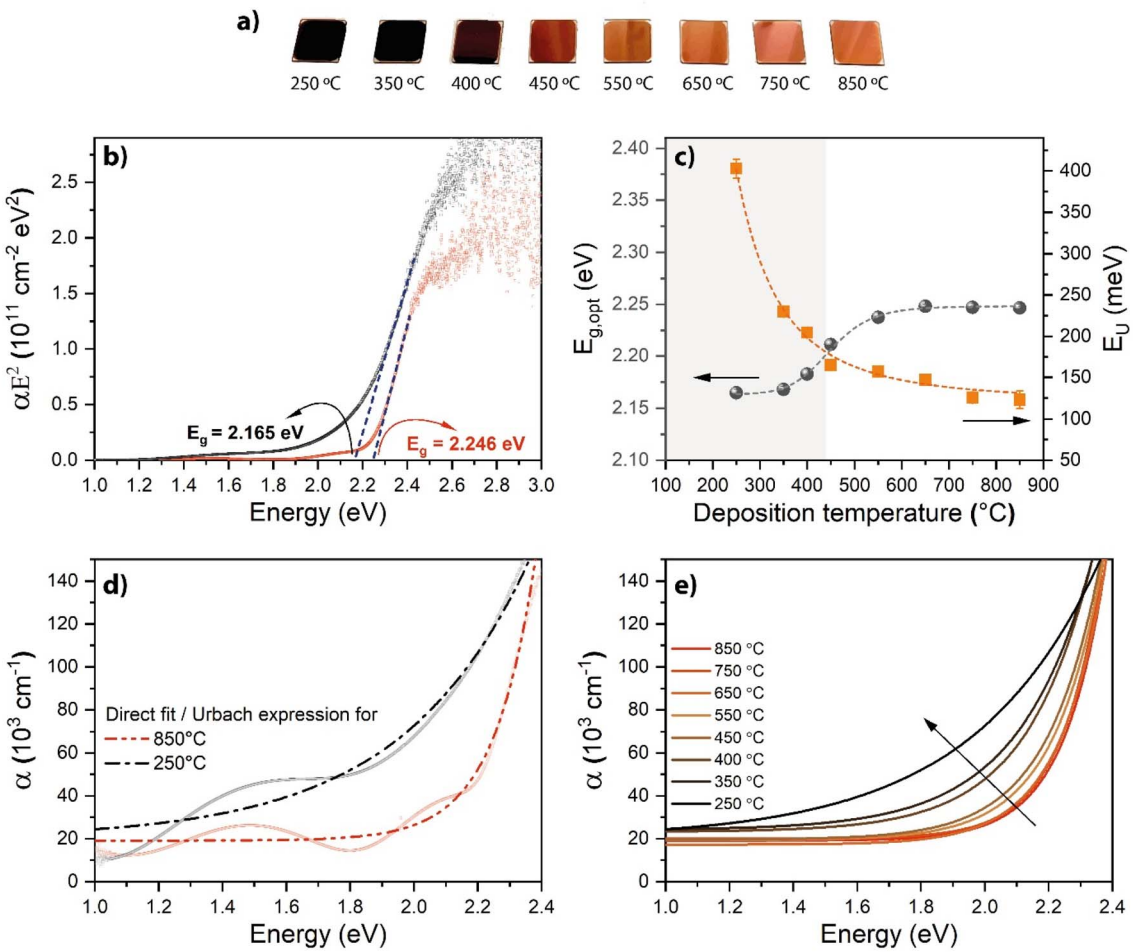

Fig. 4 (a) Photographs of the films deposited on *c*-sapphire at different temperatures displaying a variation in color noticeable by the naked eye; (b) Tauc plots of $(\alpha E)^2$ as a function of photon energy (E) for the samples grown at 850 °C (in orange) and 250 °C (in black); the dashed lines represent the tangents; (c) extracted values of the optical bandgap ($E_{g,opt}$) and Urbach energy (E_U) as a function of deposition temperature; the grey zone represents the temperature region for which the cell underwent a pronounced increase in the in-plane strain/deformation; (d) absorption coefficient (α) as a function of photon energy (E) for the samples grown at 850 °C and 250 °C; the dashed lines represent a direct fit of eqn (5) to the data; and (e) comparison between all the direct fits of eqn (5) performed to the measured $\alpha(E)$.

effects arising from internal reflections inside the films with thicknesses in the range 200–270 nm. Acknowledging the presence of interference is crucial, as neglecting it can lead to erroneous interpretations of the results. To estimate E_U, the measured $\alpha(E)$ data (not shown in the figure) were fitted with eqn (5) in the range 1.05 to 2.35 eV for all samples. The presence of interference oscillations did not affect the fit, as confirmed by an envelope-fit method, which provided similar E_U values (refer to Fig. S7, S8 and Table S4 in the SI). Fig. 4e shows the curve resulting from the direct fits, which reflect the width of the electronic states' tails that penetrated the bandgap for each sample. Reducing the growth temperature caused a notable increase in the tail's width, which led to stronger absorption in the sub-bandgap region.

The extracted E_U values along with $E_{g,opt}$ as a function of the deposition temperature are presented in Fig. 4c. The direct bandgap and Urbach energies suffered drastic changes with a decreased deposition temperature. In particular, the Urbach energy became clearly higher for temperatures below 450 °C.

The Urbach energy is associated with the degree of thermal and structural disorder in a material. Accordingly, E_U can be considered the sum of two distinct contributions: $E_U = E_T + E_S$, where E_T represents the thermal disorder ascribed to the thermal excitation of phonons, and E_S corresponds to the static structural disorder, and is related to the density of defects.[61–63] Given that all samples in this study were measured at the same temperature, E_T is assumed to be similar across all samples. Such an assumption was first proposed by Cody.[66] Therefore, the observed variations in E_U were ascribed to differences in the structural disorder between the samples, offering valuable information regarding the presence, and distribution of the energy of the defect-related electronic states in the sub-bandgap region.[62,64]

A detailed analysis of the transmittance measurements revealed that reducing the growth temperature led to a significant increase in the defect density of the ScN thin films deposited by HiPIMS. Particularly, it was observed that decreasing the growth temperature from 850 °C to 250 °C

 This journal is © The Royal Society of Chemistry 2025

Open Access Article. Published on 03 December 2025. Downloaded on 12/8/2025 11:38:25 AM.
This article is licensed under a Creative Commons Attribution 3.0 Unported Licence.

resulted in an increase of approximately 280 meV in the E_U and a simultaneous reduction of about 80 meV in the optical bandgap. This behavior is consistent with a defect-induced renormalization of the bandgap caused by the increase in the density of states related to the electronic states in the sub-bandgap region that penetrated into the bandgap, effectively narrowing it.[67] It must be noted that the high E_U values obtained in this study are compatible with the presence of the electrostatic fluctuating potentials along the semiconductor.[62,64]

3.4 Electrical and thermoelectric properties

Fig. 5 displays the temperature-dependent electrical and thermoelectric properties of the films deposited on the *c*-sapphire substrate. Three different behaviors were observed for the temperature dependence of electrical conductivity (Fig. 5a). The films deposited at high-deposition temperatures ($T_s \geq 650$ °C) exhibited typical metallic behavior and the electrical conductivity of the material was reduced with temperature. This behavior is commonly observed for a fully degenerate semiconductor and ScN materials, with values of the electrical conductivity varying between 4×10^3 and 5×10^6 S cm^{-1}.[7–9,11,13,15] The films deposited at low-deposition temperatures ($T_s \leq 450$ °C) exhibited typical semiconductor behavior with electrical conductivities that increased with temperature. Intermediate-growth temperatures led to films exhibiting electrical conductivities that were relatively constant over the large range of the measured temperatures. Overall, the electrical conductivities of the films were drastically reduced at values below 2000–3000 S cm^{-1} when the deposition temperature was below 650 °C and metallic behavior was no longer present.

The absolute Seebeck coefficient values of ScN exhibited a typical temperature-dependent behavior, which increased with an increase in the measurement temperature (Fig. 5b). The absolute Seebeck coefficient values increased progressively from 60 to 220 μV K^{-1} (at 320 K) when the growth temperature of the film was reduced, and they inversely evolved with the electrical conductivity trend.

The TE power factor was clearly dominated by the evolution of the electrical conductivity in the series of samples. The reduction of the electrical conductivity in the series of samples was too large to be compensated by the increase in the absolute Seebeck coefficient needed to maintain a decent TE power factor. The films that exhibited the maximum thermoelectric power factor were the ones deposited at 750 and 850 °C with a power factor around 1.25 mW m^{-1} K^{-2} at 320 K to over 2.0 mW m^{-1} K^{-2} at 500 K.

Further electrical characterizations were performed for determining the carrier concentration and Hall mobility near room temperature (Fig. 6). The comparison of the electrical properties obtained on the *c*-sapphire with the second series of samples deposited on the SiO_2 (200 nm)/Si substrates are presented in the SI (Fig. S9).

For the films deposited on the *c*-sapphire, the electrical conductivities of those films varied from 3000–4000 down to 0.1–1 S cm^{-1} (Fig. 6a). The carrier concentration remained

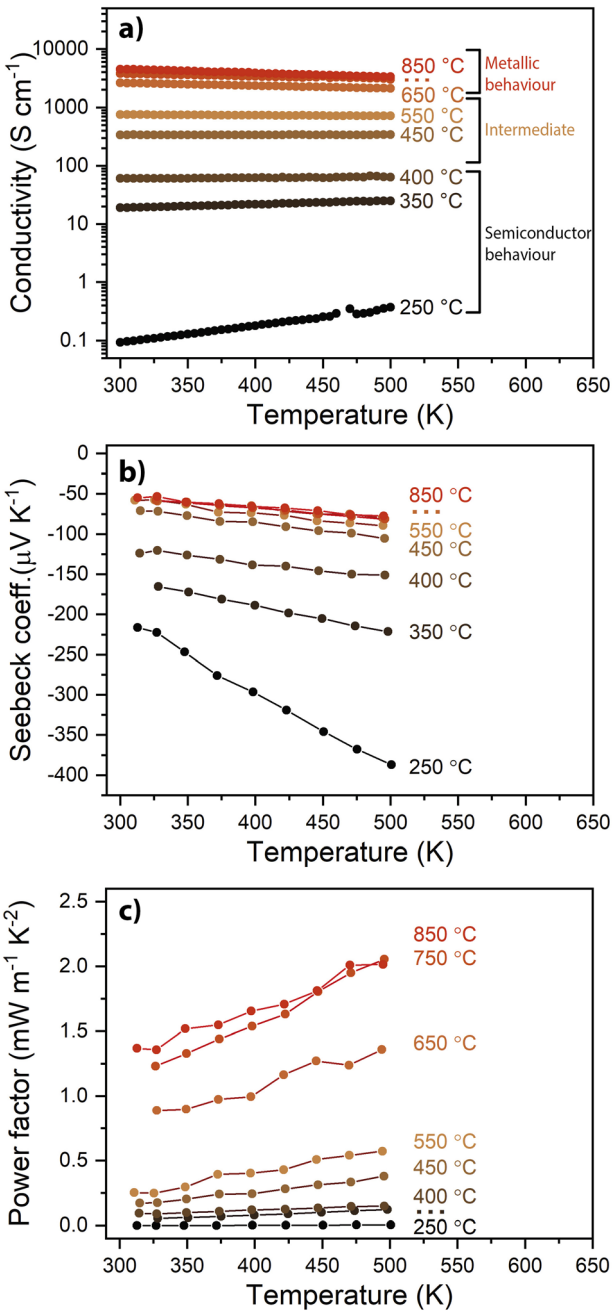

Fig. 5 Temperature-dependent electrical and thermoelectric characteristics of the films deposited at different deposition temperatures on *c*-sapphire: (a) electrical conductivity, (b) Seebeck coefficient and (c) TE power factor.

relatively the same around 4×10^{20} cm^{-3} when T_s was ≥550 °C and it was gradually reduced to 2×10^{18} cm^{-3} when the growth temperature was reduced to 250 °C. The carrier mobility evolved in a similar fashion as the carrier density after a decrease in the growth temperatures, with values decreasing from 50 to 0.2 cm^2 V^{-1} s^{-1} (Fig. 6c).

Similarly, the absolute value of the Seebeck coefficient remained constant around −50 to −60 μV K^{-1} before it drastically increased to a maximum of −225 μV K^{-1} when deposition was at the lowest temperature. For the films deposited at high

Open Access Article. Published on 03 December 2025. Downloaded on 12/8/2025 11:38:25 AM.
This article is licensed under a Creative Commons Attribution 3.0 Unported Licence.

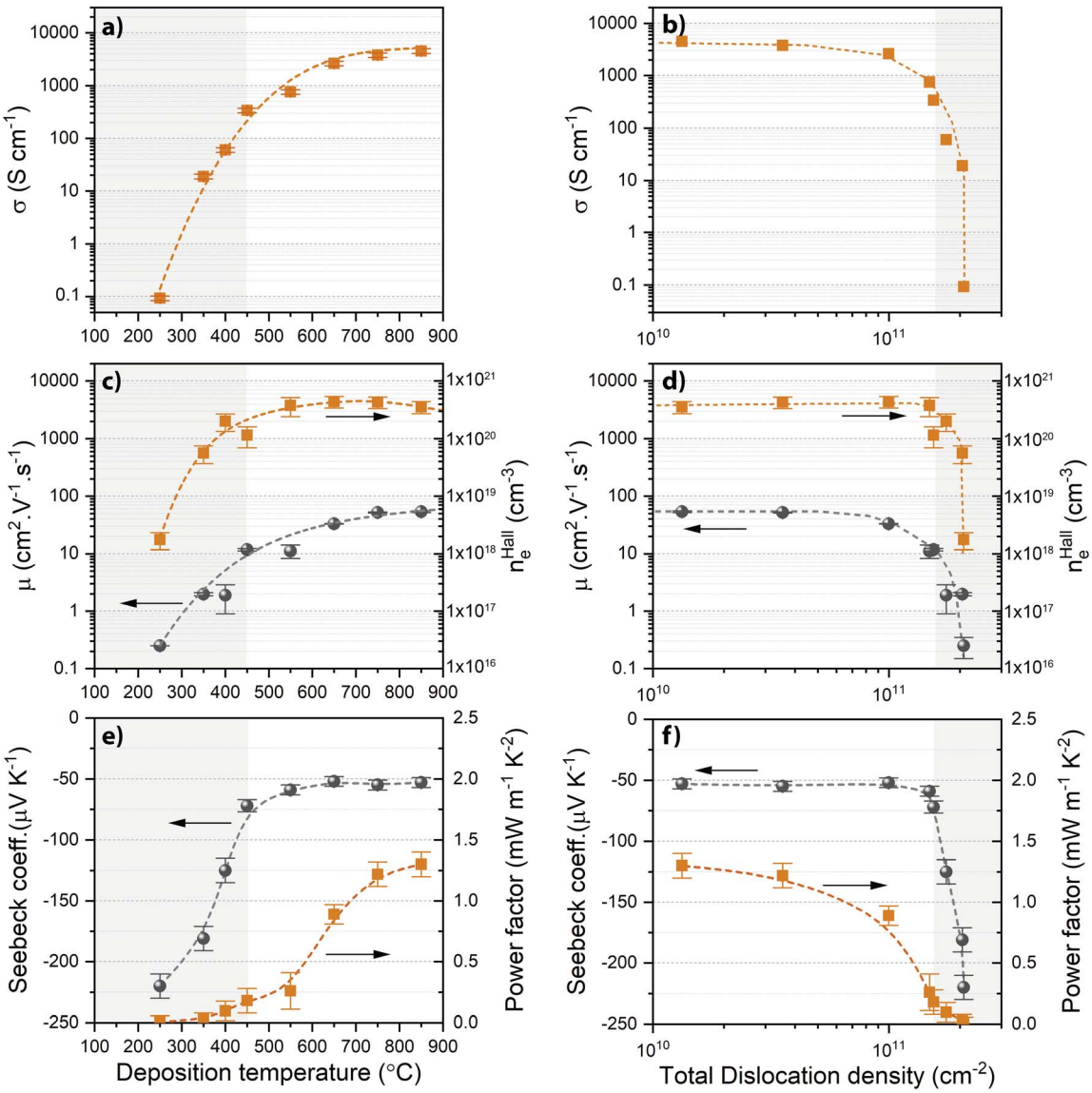

Fig. 6 Room-temperature electrical and thermoelectric properties of the films deposited on *c*-sapphire *versus* either the deposition temperature (a, c and e) or the total dislocation density (b, d and f); (a and b) electrical conductivity; (c and d) Hall carrier concentration and mobility; and (e and f) Seebeck coefficient and TE power factor. The dashed lines provide a visual guide for the trend in the series of samples, and the grey zones represent the temperature interval for which the cell underwent a pronounced increase in the in-plane strain/deformation.

temperatures, the resulting power factor was relatively high, with values around 1.3 mW m^{-1} K^{-2}. For the films grown at lower temperatures, even with larger values of the absolute Seebeck coefficient, the reduction of the electrical conductivity was too large, yielding a lower power factor below 0.01 mW m^{-1} K^{-2}.

The variation of electrical properties can be investigated from a deformation and dislocation point of view (Fig. 6b, d and f). The thermoelectric properties of ScN seemed to have degraded slowly when the total number of dislocations increased from 10^{10} to 10^{11} cm^{-2}, while above 10^{11} cm^{-2} these properties degraded rapidly, completely deteriorating the thermoelectric performance of the ScN films. This correlates well with the measured strain (Fig. 3), where the films with the maximum strain above the saturated dislocation density level (represented in the grey area in Fig. 6) also had the poorest TE properties with the lowest power factor.

On the SiO_2 (200 nm)/Si substrate (Fig. S9), the overall electrical and thermoelectric properties of the films behaved similarly to the ones observed on the *c*-sapphire. The thermoelectric performances of the films deposited on the SiO_2 (200 nm)/Si substrate was relatively larger than the ones deposited on the *c*-sapphire, exhibiting similar degradation when the growth temperature was reduced. For example, the TE power factors of the films deposited on the SiO_2 (200 nm)/Si substrate were 50% larger than the ones on the *c*-sapphire due to their larger Seebeck coefficient values, and the trend was the same on both substrates with a reduction of 100% when the growth temperature was reduced from 850 to 550 °C (Fig. S9d).

 This journal is © The Royal Society of Chemistry 2025

Open Access Article. Published on 03 December 2025. Downloaded on 12/8/2025 11:38:25 AM. This article is licensed under a Creative Commons Attribution 3.0 Unported Licence.

Post-annealing treatments were performed on the two extreme cases (lowest and highest T_s) to evaluate the stability of the defects created by HiPIMS (further details are described in Fig. S10 and Table S5 in the SI). The room-temperature electrical properties were investigated for both films after they were annealed at 1300 °C for 10 min. The film deposited at $T_s = 850$ °C did not undergo significant changes after high-temperature annealing. However, the film initially deposited at 250 °C underwent drastic changes to resemble the film initially deposited at $T_s = 850$ °C after high-temperature annealing. The color of the ScN was completely restored to its red/orange color, and the electrical properties more closely resembled the ones measured initially on the as-deposited film at 850 °C (Table S3). These findings support the hypothesis that the film deposited at low temperatures by HiPIMS contains a large density of defects, which (i) seem to originate from the residual stress and create dislocations and distortions in the cubic ScN material, (ii) deteriorate the electrical and thermoelectric properties of the degenerate semiconductor, and (iii) can be completely eliminated after a high-temperature annealing step.

4 Discussion

The thermoelectric properties of ScN seem to have been affected by the deposition temperature of the films. In this present case, no variations were detected for the film compositions, and in the XPS signature of ScN regardless of T_s. Nevertheless, T_s had a significant effect on strain, and dislocation formation in the films. The HiPIMS-induced energetic ion bombardment during deposition often led to the creation of residual strain. In the case of ScN, the residual strain impacted the electrical transport and thermoelectric properties of the final films, leading to overall degradation of the degenerate semiconductor. The variation in the electrical transport and thermoelectric properties seems to be interdependent on the carrier concentration, given the parabolic band, energy-independent scattering approximation, which is valid for metals and degenerate semiconductors:[12,68]

$$S = \frac{8\pi^2 {k_B}^2}{3eh^2} m^* T \left(\frac{\pi}{3n}\right)^{2/3} \quad (6)$$

and

$$\sigma = n\mu e \quad (7)$$

where n is the carrier concentration, m^* is the effective mass, σ the electrical conductivity and μ the carrier mobility. Indeed, when the deposition temperature was decreased, there was a decrease in the charge carrier concentration, yielding an increase of the absolute Seebeck coefficient and a simultaneous decrease in the electrical conductivity (Fig. 6).

Several parameters could have potentially caused a reduction of the carrier concentration that occurred when the temperature was reduced. In ScN, the thermoelectric properties can be affected by the stoichiometry of ScN, oxygen contamination, the orientation of the film, the residual stress, and point defects. In the present case, the film composition and orientation did not change with T_s and are excluded from further discussion herein as their impact was minimal. The parameters that had a major impact were the residual strain and related consequences from the creation of dislocations, possible point defects, and lattice distortion. The RSM analysis of the films revealed that there was a higher dislocation density when the temperature decreased to the saturation level obtained for $T_s < 450$ °C. Below that temperature, an overall distortion of the cell occurred, resulting in a rhombohedral distortion of the cubic cell ($\alpha = \beta = \gamma \neq 90$, and $a = b = c$). An increase of stress in the films would have caused the formation of dislocations that maintained the structural integrity of the materials. The formation of dislocations occurred in the series of films to minimize strain and the deformation of the cell to a point ($T_s = 450$ °C). Below that temperature, the materials cannot sustain the strain levels and no further dislocations were created, but rather distortions of the materials occurred. This was further corroborated by the significant decrease in carrier mobility, indicating that the defects, particularly dislocations, altered the hierarchy of the scattering mechanisms, with these defects clearly dominating carrier scattering at low-deposition temperatures.

The theoretical DFT calculations were performed to retrieve the electronic band structure of the unstressed ScN and the distorted, experimentally measured ScN that was grown at the lowest temperature. A visual representation of those electronic band structures is presented in the SI (Fig. S11). The electronic band structure obtained for the unstressed ScN was similar to values reported in the literature[69–71] with an indirect bandgap estimated at 0.827 eV between the X–Γ points and the direct bandgaps estimated at 3.5 eV at the Γ point and 1.9 eV at the X point (Fig. S11). The electronic band structure of the distorted ScN was computed using the experimental values obtained from the RSM analysis ($a = b = c = 4.62$ Å; $\alpha = \beta = \gamma = 88.6°$) (Fig. S9). A simple rhombohedral distortion would not have drastically changed the band structure of ScN, but should have rather yielded a small increase of 0.1 eV for the direct bandgaps. Those theoretical calculations, which considered a simple rhombohedral distortion of the cell, seemed to not correlate with the experimental data, where a reduction of 0.1 eV for the optical bandgap was observed and the film became more insulating when grown at low temperature.

From the optical transmission measurements, a decrease of the bandgap was observed along with an increase in the Urbach energy for the films deposited at $T_s < 450$ °C. This increase in the Urbach energy strongly reflected the increase of the absorption tail into the bandgap. This shows that electronic transitions involving defect states in the bandgap near the edges of the valence band and conduction bands occurred. As the growth temperature was reduced, the Urbach energy increased, and hence, the increase of the density of the electronic states near the band edges was compatible with a higher density of defects (dislocations and point defects), which was more pronounced when the films were under a high level of residual strain.

The high values of E_U are an indicator of lattice disorder, which consequently led to the poor electrical properties, where the free-carrier mobility as well as the concentration of free charge carriers were drastically reduced. Defect-related electronic levels seemed to

Open Access Article. Published on 03 December 2025. Downloaded on 12/8/2025 11:38:25 AM. This article is licensed under a Creative Commons Attribution 3.0 Unported Licence.

have been induced near the valence or conduction band edges, contributing to the bandgap narrowing, the creation of trap levels, and a reduction in the concentration of free charge carriers, ultimately affecting/degrading the thermoelectric performance of the ScN films. The lattice disorder responsible for high E_U was clearly identified here by the creation of crystal defects including: dislocations, lattice distortion that occurred during film growth and its dominance at low temperatures ($T_s \leq 450$ °C). However, the presence of point defects cannot be entirely excluded and can play a similar role as the other crystal defects in the creation of trap levels near the bandgap. In the present series of samples, two regimes can be identified: (i) a "dislocation" regime and (ii) a "strain/distortion" regime, with a small and a large effect, respectively, on the optical and electric properties. From the point of view of thermoelectric applications, and for ScN, a sharpening of the band tails is desirable since it lowers trap densities as well as deep recombination centers.

The energetic metal ion bombardment by HiPIMS has been utilized as a great tool for reducing the growth temperature. In this present case, the use of HiPIMS allowed the deposition of ScN films with the right stoichiometry, low oxygen contamination and a relatively high crystalline quality even at low growth temperatures. However, the films grown at low-deposition temperatures (T_s < 450 °C) exhibited a relatively high strain level, which was observable in the overall cell deformation and high dislocation density. These defects and stress level yielded a deterioration of the thermoelectric properties of the films.

The mechanism we propose for explaining the observed changes of the thermoelectric properties due to HiPIMS-induced defects is as follows: all the films in this study were grown at a V_{float} (the energy of the ions bombarding the growing film surface) value of around ~25 eV for the singly charged metal and gas ions, and it was ~50 eV for the doubly charged ions (mostly Sc^{2+} and Ar^{2+}), which are typically at lower percentages compared to the singly charged ions. The addition of metal ions to the gas ion flux (for the dcMS-growth) enhanced the probability of defect formation as the lattice displacement energy thresholds for most transition metal nitrides are within 20–50 eV.[72] At higher deposition temperatures, the thermal energy assisted in annihilating the defects created by the energetic ion bombardment in the films. Therefore, similar thermoelectric performances of the HiPIMS-grown ScN films as that of the dcMS- grown films at equivalent temperatures (700–900 °C) were obtained.

At lower growth temperatures, the thermal energy was insufficient for removing the defects higher dislocation density and deformation (Fig. 3), hence it did not have an important impact on the electrical and thermoelectric properties. However, its ability to maintain the film stoichiometry at any growth temperature gives HiPIMS an advantage over the conventional dcMS method, where obtaining a N/Sc ratio close to unity is not necessarily easy.[6,8–10,15,73] The negative impact of the stress/strain generated in HiPIMS-grown ScN at low temperatures can be mitigated by selective metal-ion irradiation. This would provide the ability to tailor the strain levels and would be the key to the successful growth of degenerate semiconductors at low temperature using HiPIMS.

5 Conclusion

In conclusion, in the series of ScN films grown at different temperatures, different stages of defects and strain were achieved for ScN, while the composition of the film was maintained close to stoichiometry. The structural variations of the films led to various changes in the properties of the films, highlighting the sensitivity of ScN to structural and point defects. ScN exhibited degenerate semiconductor behavior with high-performance thermoelectric properties compared to a more classical semiconductor behavior and poor thermoelectric properties. These differences were explained by the presence of crystal defects (dislocations and point defects) in the films, which created defect states near the edges of the valence and conduction bands that impacted the electron density and mobility, and ultimately the correlated electrical transport and thermoelectric properties. The use of high-power impulse magnetron sputtering and more energetic adatoms when growing the films allowed for the control of the electrical and optical properties of the films through strain/defect engineering. These findings highlight the significance of strain in influencing thermoelectric properties, suggesting that it can serve as a pathway for enhancing the thermoelectric properties of other materials or more complex thin film configurations. This study also highlights the high potential of HiPIMS, which can be further used and optimized to control the density of defects created in films and/or reduce the growth temperature with minimum defect densities, while maintaining the degenerate semiconducting properties of ScN.

Author contributions

ALF: conceptualization, data curation, formal analysis, investigation, methodology, validation, visualization, project administration, supervision, writing – original draft, writing – review & editing. SKH: data curation, formal analysis, methodology, writing – review & editing. CP: data curation, formal analysis, investigation, validation, visualization. TVF: data curation, formal analysis, investigation, validation, visualization, writing – review & editing. RF: data curation, investigation, validation. VR: data curation, investigation, validation. MM: data curation, investigation, validation, visualization. FG: data curation, formal analysis, validation. JPL: funding acquisition, resources, writing – review & editing. J-FB: funding acquisition, resources, supervision, writing – review & editing. PE: funding acquisition, resources, supervision, writing – review & editing.

Conflicts of interest

The authors declare no competing financial interest.

Data availability

Data supporting this article have been included as part of the supplementary information (SI). Further data will be available on request. Supplementary information: SI corroborates the findings with films deposited under identical conditions on an SiO_2(200 nm)/Si substrate. It further includes comprehensive

 This journal is © The Royal Society of Chemistry 2025

Open Access Article. Published on 03 December 2025. Downloaded on 12/8/2025 11:38:25 AM. This article is licensed under a Creative Commons Attribution 3.0 Unported Licence.

characterization of the compositional analysis employing techniques such as Time-of-Flight Elastic Recoil Detection Analysis (ToF-ERDA) and X-ray Photoelectron Spectroscopy (XPS), as well as structural characterization through X-ray Diffraction (XRD), including X-ray Reflectivity (XRR) and X-ray pole figure analysis for both substrate types. Additionally, the supplemental section addresses optical characterizations with detailed analysis of transmission data, comparative assessments of electrical properties between the two substrate types, effects of post-annealing treatments, and a theoretical Density Functional Theory (DFT) calculation that delineates the electronic band structure of both unstrained and strained ScN. See DOI: https://doi.org/10.1039/d5ta07228j.

Acknowledgements

The authors acknowledge Ching-Lien Hsiao for lending the HiPSTER 1 HiPIMS power supplies for the deposition. The authors acknowledge funding from the Swedish Government Strategic Research Area in Materials Science on Functional Materials at Linköping University (faculty grant SFO-Mat-LiU no 2009 00971), the Knut and Alice Wallenberg foundation through the Wallenberg Academy Fellows program (KAW-2020.0196), the Swedish Research Council (VR) under project no 2021-03826. M.M. acknowledges financial support from the Swedish Energy Agency (grant no. 43606-1) and the Carl Tryggers Foundation (CTS23:2746, CTS20:272, CTS16:303, and CTS14:310). This work was supported by the French government program "Investissements d'Avenir" (EUR INTREE – reference ANR-18-EURE-0010, LABEX INTERACTIFS – reference ANR-11-LABEX-0017-01, and UP-SQUARED – reference ANR-21-EXES-0013). Daniel Primetzhofer from Uppsala University is acknowledged for Accelerator operation supported by the Swedish Research Council VR-RFI (contract no 2019-00191) and the Swedish Foundation for Strategic Research (contract no. RIF14-0053). Joaquim Leitão acknowledges the financial support by national funds through the FCT-Fundação para a Ciência e a Tecnologia, I.P., within the scope of project UID/50025/2025 (10.54499/UID/50025/2025) and the Associate Laboratory I3N – LA/P/0037/2020 (10.54499/LA/P/0037/2020).

References

1 B. Biswas and B. Saha, Development of semiconducting ScN, *Phys. Rev. Mater.*, 2019, **3**, 020301.
2 P. Eklund, S. Kerdsongpanya and B. Alling, Transition-metal-nitride-based thin films as novel energy harvesting materials, *J. Mater. Chem. C*, 2016, **4**, 3905–3914.
3 P. John, *et al.*, ScN/GaN(1$\bar{1}$00): A New Platform for the Epitaxy of Twin-Free Metal-Semiconductor Heterostructures, *Nano Lett.*, 2024, **24**, 6233–6239.
4 M. J. Kappers, M. A. Moram, Y. Zhang, M. E. Vickers, Z. H. Barber and C. J. Humphreys, Interlayer methods for reducing the dislocation density in gallium nitride, *Phys. B*, 2007, **401–402**, 296–301.
5 M. A. Moram, Y. Zhang, M. J. Kappers, Z. H. Barber and C. J. Humphreys, Dislocation reduction in gallium nitride films using scandium nitride interlayers, *Appl. Phys. Lett.*, 2007, **91**, 152101.
6 N. Tureson, *et al.*, Reduction of the thermal conductivity of the thermoelectric material ScN by Nb alloying, *J. Appl. Phys.*, 2017, **122**, 025116.
7 D. Rao, *et al.*, High mobility and high thermoelectric power factor in epitaxial ScN thin films deposited with plasma-assisted molecular beam epitaxy, *Appl. Phys. Lett.*, 2020, **116**, 152103.
8 J. More-Chevalier, *et al.*, Enhancing thermoelectric properties of ScN films through twin domains, *Appl. Surf. Sci. Adv.*, 2025, **25**, 100674.
9 S. Kerdsongpanya, *et al.*, Anomalously high thermoelectric power factor in epitaxial ScN thin films, *Appl. Phys. Lett.*, 2011, **99**, 232113.
10 P. V. Burmistrova, *et al.*, Effect of deposition pressure on the microstructure and thermoelectric properties of epitaxial ScN(001) thin films sputtered onto MgO(001) substrates, *J. Mater. Res.*, 2015, **30**, 626–634.
11 P. V. Burmistrova, *et al.*, Thermoelectric properties of epitaxial ScN films deposited by reactive magnetron sputtering onto MgO(001) substrates, *J. Appl. Phys.*, 2013, **113**, 153704.
12 G. J. Snyder and E. S. Toberer, Complex thermoelectric materials, *Nat. Mater.*, 2008, **7**, 105–114.
13 B. Saha, G. Naik, V. P. Drachev, A. Boltasseva, E. E. Marinero and T. D. Sands, Electronic and optical properties of ScN and (Sc,Mn)N thin films deposited by reactive DC-magnetron sputtering, *J. Appl. Phys.*, 2013, **114**, 063519.
14 Y. Oshima, E. G. Víllora and K. Shimamura, Hydride vapor phase epitaxy and characterization of high-quality ScN epilayers, *J. Appl. Phys.*, 2014, **115**, 153508.
15 A. le Febvrier, N. Tureson, N. Stilkerich, G. Greczynski and P. Eklund, Effect of impurities on morphology, growth mode, and thermoelectric properties of (1 1 1) and (0 0 1) epitaxial-like ScN films, *J. Phys. D: Appl. Phys.*, 2019, **52**, 035302.
16 S. Kerdsongpanya, B. Alling and P. Eklund, Effect of point defects on the electronic density of states of ScN studied by first-principles calculations and implications for thermoelectric properties, *Phys. Rev. B*, 2012, **86**, 195140.
17 J. R. Sootsman, *et al.*, Large Enhancements in the Thermoelectric Power Factor of Bulk PbTe at High Temperature by Synergistic Nanostructuring, *Angew. Chem., Int. Ed.*, 2008, **47**, 8618–8622.
18 B. Poudel, *et al.*, High-Thermoelectric Performance of Nanostructured Bismuth Antimony Telluride Bulk Alloys, *Science*, 2008, **320**, 634–638.
19 J. M. Gregoire, S. D. Kirby, G. E. Scopelianos, F. H. Lee and R. B. Dover, High mobility single crystalline ScN and single-orientation epitaxial YN on sapphire *via* magnetron sputtering, *J. Appl. Phys.*, 2008, **104**, 074913.
20 D. Gall, I. Petrov, P. Desjardins and J. E. Greene, Microstructural evolution and Poisson ratio of epitaxial ScN grown on TiN(001)/MgO(001) by ultrahigh vacuum reactive magnetron sputter deposition, *J. Appl. Phys.*, 1999, **86**, 5524–5529.

Open Access Article. Published on 03 December 2025. Downloaded on 12/8/2025 11:38:25 AM. This article is licensed under a Creative Commons Attribution 3.0 Unported Licence.

21 G. Greczynski, J. Jensen, J. Böhlmark and L. Hultman, Microstructure control of CrNx films during high power impulse magnetron sputtering, *Surf. Coat. Technol.*, 2010, **205**, 118–130.
22 J. Patidar, *et al.*, Improving the crystallinity and texture of oblique-angle-deposited AlN thin films using reactive synchronized HiPIMS, *Surf. Coat. Technol.*, 2023, **468**, 129719.
23 L. Lapeyre, *et al.*, Deposition and characterisation of *c*-axis oriented AlScN thin films *via* microwave plasma-assisted reactive HiPIMS, *Surf. Coat. Technol.*, 2023, **464**, 129540.
24 J. Patidar, K. Thorwarth, T. Schmitz-Kempen, R. Kessels and S. Siol, Deposition of highly crystalline AlScN thin films using synchronized high-power impulse magnetron sputtering: From combinatorial screening to piezoelectric devices, *Phys. Rev. Mater.*, 2024, **8**, 095001.
25 J. Bohlmark, *et al.*, The ion energy distributions and ion flux composition from a high power impulse magnetron sputtering discharge, *Thin Solid Films*, 2006, **515**, 1522–1526.
26 T. Kubart, M. Čada, D. Lundin and Z. Hubička, Investigation of ionized metal flux fraction in HiPIMS discharges with Ti and Ni targets, *Surf. Coat. Technol.*, 2014, **238**, 152–157.
27 M. M. S. Villamayor, *et al.*, Low temperature (Ts/Tm < 0.1) epitaxial growth of HfN/MgO(001) *via* reactive HiPIMS with metal-ion synchronized substrate bias, *J. Vac. Sci. Technol., A*, 2018, **36**, 061511.
28 S. K. Honnali, *et al.*, Epitaxial growth of TiZrNbTaN films without external heating by high-power impulse magnetron sputtering, *Surf. Coat. Technol.*, 2025, **495**, 131583.
29 X. Li, B. Bakhit, M. P. Johansson Jõesaar, I. Petrov, L. Hultman and G. Greczynski, Dense, single-phase, hard, and stress-free Ti0.32Al0.63W0.05N films grown by magnetron sputtering with dramatically reduced energy consumption, *Sci. Rep.*, 2022, **12**, 2166.
30 J. Vetter, *et al.*, Industrial application potential of high power impulse magnetron sputtering for wear and corrosion protection coatings, *J. Appl. Phys.*, 2023, **134**, 160701.
31 N. Zinai, *et al.*, Tailoring the structural and optical properties of HiPIMS TiO2 thin films for photovoltaic applications, *Opt. Mater.*, 2022, **131**, 112590.
32 P. Kumar, G. M. Seema and S. Avasthi, Fully dense, highly conductive nanocrystalline TiN diffusion barrier on steel *via* reactive high power impulse magnetron sputtering, *Thin Solid Films*, 2021, **722**, 138578.
33 T. Shimizu, M. Villamayor, D. Lundin and U. Helmersson, Process stabilization by peak current regulation in reactive high-power impulse magnetron sputtering of hafnium nitride, *J. Phys. D: Appl. Phys.*, 2016, **49**, 065202.
34 G. Greczynski, J. Jensen and L. Hultman, $\hbox{CrN}_{\rm x}$ Films Prepared by DC Magnetron Sputtering and High-Power Pulsed Magnetron Sputtering: A Comparative Study, *IEEE Trans. Plasma Sci.*, 2010, **38**, 3046–3056.
35 J. C. Sánchez-López, A. Caro, G. Alcalá and T. C. Rojas, Tailoring CrNx stoichiometry and functionality by means of reactive HiPIMS, *Surf. Coat. Technol.*, 2020, **401**, 126235.
36 M. Samuelsson, D. Lundin, J. Jensen, M. A. Raadu, J. T. Gudmundsson and U. Helmersson, On the film density using high power impulse magnetron sputtering, *Surf. Coat. Technol.*, 2010, **205**, 591–596.
37 D. J. Christie, Target material pathways model for high power pulsed magnetron sputteringa, *J. Vac. Sci. Technol., A*, 2005, **23**, 330–335.
38 R. Machunze and G. C. A. M. Janssen, Stress and strain in titanium nitride thin films, *Thin Solid Films*, 2009, **517**, 5888–5893.
39 F. Cemin, G. Abadias, T. Minea and D. Lundin, Tuning high power impulse magnetron sputtering discharge and substrate bias conditions to reduce the intrinsic stress of TiN thin films, *Thin Solid Films*, 2019, **688**, 137335.
40 A. le Febvrier, L. Landälv, T. Liersch, D. Sandmark, P. Sandström and P. Eklund, An upgraded ultra-high vacuum magnetron-sputtering system for high-versatility and software-controlled deposition, *Vacuum*, 2021, **187**, 110137.
41 S. K. Honnali, C. Poterie, A. le Febvrier, D. Lundin, G. Greczynski and P. Eklund, Effect of tilted closed-field magnetron design on the microstructure and mechanical properties of TiZrNbTaN coatings, *J. Vac. Sci. Technol., A*, 2023, **41**, 043402.
42 C. Comparotto, P. Ström, O. Donzel-Gargand, T. Kubart and J. J. S. Scragg, Synthesis of BaZrS3 Perovskite Thin Films at a Moderate Temperature on Conductive Substrates, *ACS Appl. Energy Mater.*, 2022, **5**, 6335–6343.
43 K. Arstila, *et al.*, Potku – New analysis software for heavy ion elastic recoil detection analysis, *Nucl. Instrum. Methods Phys. Res., Sect. B*, 2014, **331**, 34–41.
44 G. Kresse and J. Furthmüller, Efficient iterative schemes for *ab initio* total-energy calculations using a plane-wave basis set, *Phys. Rev. B*, 1996, **54**, 11169–11186.
45 G. Kresse and D. Joubert, From ultrasoft pseudopotentials to the projector augmented-wave method, *Phys. Rev. B*, 1999, **59**, 1758–1775.
46 P. E. Blöchl, Projector augmented-wave method, *Phys. Rev. B*, 1994, **50**, 17953–17979.
47 J. Heyd, G. E. Scuseria and M. Ernzerhof, Hybrid functionals based on a screened Coulomb potential, *J. Chem. Phys.*, 2003, **118**, 8207–8215.
48 A. V. Krukau, O. A. Vydrov, A. F. Izmaylov and G. E. Scuseria, Influence of the exchange screening parameter on the performance of screened hybrid functionals, *J. Chem. Phys.*, 2006, **125**, 224106.
49 J. More-Chevalier, *et al.*, Correlation between crystallization and oxidation process of ScN films exposed to air, *Appl. Surf. Sci.*, 2020, **515**, 145968.
50 S. Chowdhury, *et al.*, Detailed study of reactively sputtered ScN thin films at room temperature, *Materialia*, 2022, **22**, 101375.
51 W. Lengauer, Investigations in the scandium-nitrogen system, *J. Solid State Chem.*, 1988, **76**, 412–415.
52 A. F. Lahiji F, B. Paul, A. le Febvrier and P. Eklund, Unusual tilted growth and epitaxial relationship of NaCl B1-

 This journal is © The Royal Society of Chemistry 2025

Open Access Article. Published on 03 December 2025. Downloaded on 12/8/2025 11:38:25 AM.
This article is licensed under a Creative Commons Attribution 3.0 Unported Licence.

structured NiO and CrN on r-plane Al2O3, *J. Appl. Phys.*, 2024, **135**, 065302.
53 R. Niewa, D. A. Zherebtsov, M. Kirchner, M. Schmidt and W. Schnelle, New Ways to High-Quality Bulk Scandium Nitride, *Chem. Mater.*, 2004, **16**, 5445–5451.
54 M. A. Moram and M. E. Vickers, X-ray diffraction of III-nitrides, *Rep. Prog. Phys.*, 2009, **72**, 036502.
55 C. G. Dunn and E. F. Kogh, Comparison of dislocation densities of primary and secondary recrystallization grains of Si-Fe, *Acta Metall.*, 1957, **5**, 548–554.
56 J. Tauc and A. Menth, States in the gap, *J. Non-Cryst. Solids*, 1972, **8–10**, 569–585.
57 N. Ghobadi, Band gap determination using absorption spectrum fitting procedure, *Int. Nano Lett.*, 2013, **3**, 2.
58 Z. Chen, *et al.*, UV-vis Spectroscopy, in. *Photoelectrochemical Water Splitting: Standards, Experimental Methods, and Protocols*, ed. Chen Z., Dinh H. N. and Miller E., Springer, New York, 2013.
59 H. C. Casey Jr and F. Stern, Concentration-dependent absorption and spontaneous emission of heavily doped GaAs, *J. Appl. Phys.*, 1976, **47**, 631–643.
60 F. Urbach, The Long-Wavelength Edge of Photographic Sensitivity and of the Electronic Absorption of Solids, *Phys. Rev.*, 1953, **92**, 1324.
61 G. D. Cody, T. Tiedje, B. Abeles, B. Brooks and Y. Goldstein, Disorder and the Optical-Absorption Edge of Hydrogenated Amorphous Silicon, *Phys. Rev. Lett.*, 1981, **47**, 1480–1483.
62 J. P. Teixeira, P. M. P. Salomé, B. Alves, M. Edoff and J. P. Leitão, Evidence of Limiting Effects of Fluctuating Potentials on V_{OC} of Cu(In,Ga)Se_2 Thin-Film Solar Cells, *Phys. Rev. Appl.*, 2019, **11**, 054013.
63 M. P. Gorishnyi, Determination of the Urbach energy Eu and the optical band gap Eg of submicron C60 and C70 fullerene films, *Low Temp. Phys.*, 2025, **51**, 174–181.
64 E. Ugur, M. Ledinský, T. G. Allen, J. Holovský, A. Vlk and S. De Wolf, Life on the Urbach Edge, *J. Phys. Chem. Lett.*, 2022, **13**, 7702–7711.
65 A. S. Ferlauto, *et al.*, Analytical model for the optical functions of amorphous semiconductors from the near-infrared to ultraviolet: Applications in thin film photovoltaics, *J. Appl. Phys.*, 2002, **92**, 2424–2436.
66 G. D. Cody, Urbach edge of crystalline and amorphous silicon: a personal review, *J. Non-Cryst. Solids*, 1992, **141**, 3–15.
67 A. Walsh, J. L. F. Da Silva and S.-H. Wei, Origins of band-gap renormalization in degenerately doped semiconductors, *Phys. Rev. B*, 2008, **78**, 075211.
68 M. Cutler, J. F. Leavy and R. L. Fitzpatrick, Electronic Transport in Semimetallic Cerium Sulfide, *Phys. Rev.*, 1964, **133**, A1143–A1152.
69 S. Karki, V. Rogers, P. Jadaun, D. S. Marshall and J. A. C. Incorvia, Large Magnetoresistance in Scandium Nitride Magnetic Tunnel Junctions Using First Principles, *Adv. Theory Simul.*, 2021, **4**, 2100309.
70 J. Liu, *et al.*, Electronic structures and optical properties of two-dimensional ScN and YN nanosheets, *J. Appl. Phys.*, 2014, **115**.
71 S. Tamleh, G. Rezaei and J. Jalilian, Stress and strain effects on the electronic structure and optical properties of ScN monolayer, *Phys. Lett. A*, 2018, **382**, 339–345.
72 G. Greczynski, *et al.*, Extended metastable Al solubility in cubic VAlN by metal-ion bombardment during pulsed magnetron sputtering: film stress *vs.* subplantation, *J. Appl. Phys.*, 2017, **122**.
73 R. T. Haasch, T.-Y. Lee, D. Gall, J. E. Greene and I. Petrov, Epitaxial ScN(001) Grown and Analyzed *In situ* by XPS and UPS. I. Analysis of As-deposited Layers, *Surf. Sci. Spectra*, 2000, **7**, 169–177.